Journal of Materials Chemistry A

ROYAL SOCIETY OF CHEMISTRY

PAPER

View Article Online
View Journal | View Issue

Cite this: J. Mater. Chem. A, 2024, 12, 1685

A synergetic enhancement strategy of light utilization and carrier transfer for UV photodetection associated with artificial resonance nano-cavities†

Zhenpeng Cheng,[a] Zeping Li,[a] Ming-Yu Li, *[a] Xiaoyan Wen,[a] Xumin Ding,[b] Hao Xu,[c] Jihoon Lee,[d] Haifei Lu*[a] and Sisi Liu *[a]

Low-dimensional wide bandgap semiconductors demonstrate great potential in the large-scale fabrication of new-generation ultraviolet (UV) photodetectors (PDs) with an excellent combination of the integration level and easily tunable response spectra. However, the thickness dependence on the defect density and light absorption negatively affects the carrier photogeneration and transportation in photoactive layers, hindering the simultaneous realization of high sensitivity and low noise during detection. Herein, artificial resonance nano-cavities of 0D/2D ZnO quantum dot (QD)/MXene nanosheet (NS) composite thin films on a distributed Bragg reflector (DBR) are proposed toward high-performance UV photodetection. The uniformly distributed MXene NSs can concentrate incident photons within the composite thin films *via* boosted near-surface electromagnetic fields, and the extraction and transfer processes of photoinduced carriers are subsequently accelerated as experimentally and theoretically evidenced. The spatial light coupling between MXene NSs and the DBR with well-balanced periods of two dielectric layers further compensates for the unfavorable light–matter interaction within the 0D/2D composite thin films induced by the noticeable light transmission, and the comprehensive enhancement in the whole photocurrent generation procedure instantaneously endows the device with outstanding EQE (489.1%) and D^* (1.7×10^{13} jones), which opens a practicable route for the fabrication of UV photodetectors with exceptional optoelectronic response and long-term stability.

Received 17th October 2023
Accepted 2nd December 2023

DOI: 10.1039/d3ta06308a

rsc.li/materials-a

Introduction

Ultraviolet (UV) photodetection, a crucial technique for constructing sensing networks with an excellent anti-interference ability, has rapidly evolved in extensive applications, such as optical communication, fire warning, environmental testing, chemical/biological analysis, and national security.[1–5] Wide bandgap semiconductors are of great importance for realizing UV photodetection by converting short-wavelength electromagnetic (EM) irradiation into excited carriers, and therefore tremendous efforts have successively been devoted to developing several photoactive materials including ZnO, SiC, Ga_2O_3, GaN, and TiO_2.[6–12] Among those semiconductors, ZnO has been regarded as a competitive nominee for the implementation of UV photodetection owing to its excellent advantages, *i.e.*, a wide direct bandgap (~3.37 eV), high exciton binding energy (~60 meV), small electron and hole collision ionization coefficient, non-toxic nature, *etc.*[13–16] To meet the requirements for photodetection technique innovations, liquid-phase deposition for low-dimensional ZnO, especially for colloidal quantum dots (CQDs), has been developed for concurrently realizing energy-efficient manufacture, lattice matching, and an adjustable bandgap during the fabrication of photoactive layers.[17–19] However, the inherently irreconcilable contradiction of the inverse relationship between light absorption and carrier transportation is critically determined by the thickness of photoactive layers, which has still remained a big concern for a facile strategy.[20,21]

Localized surface plasmon resonance (LSPR) arises from the voluntarily collective oscillation of free electrons near the surface of metallic nanostructures, providing a feasible method for concentrating incident light at a characteristic extinction band.[22] Thus, improving the light utilization of optoelectronic

[a]School of Science, Wuhan University of Technology, Wuhan, 430070, China. E-mail: mingyuli.oliver@gmail.com; haifeilv@whut.edu.cn; liusisi0109@hotmail.com
[b]Advanced Microscopy and Instrumentation Research Center, School of Instrumentation Science and Engineering, Harbin Institute of Technology, Heilongjiang, 150001, China
[c]School of Physics, University of Electronic Science and Technology of China, Chengdu, 611731, China
[d]Department of Electronic Engineering, College of Electronics and Information, Kwangwoon University, Nowon-gu, Seoul 01897, Republic of Korea

† Electronic supplementary information (ESI) available. See DOI: https://doi.org/10.1039/d3ta06308a

applications has attracted extensive attention since it was experimentally evidenced with silver in 1974.[23] Recently, a new category of metalloid wo-dimensional (2D) transition metal carbides and nitrides, termed MXene, has been reported as an adequate surface plasmon polariton because of the abundant electrons and wideband high absorption.[24] Besides, the synthesis of $Ti_3C_2T_x$ MXene nanosheets (NSs) has been well-developed based on the minimally intensive layer delamination (MILD) method,[25] and their outstanding dispersibility in diverse chemical solutions is potentially beneficial for blending into ZnO thin films with an extended interface contact area for light confinement.[26,27] Nevertheless, the laminated morphology of MXene NSs with a thickness of ~1 nm can unfortunately impede the light confinement effect due to the inevitably transmitted numerous photons.[28] Constructing artificial resonance nano-cavities by introducing a reflection layer can be an alternative choice to boost the light–matter interaction of MXene NSs with a prolonged optical path. To date, various metallic reflectors have been implemented for the fabrication of photodetectors under photoactive layers: for instance, an Au back reflector has been utilized to compensate for the severe light transmission from black phosphorus layers,[29] and the light utilization of MoS_2–BP–MoS_2 heterostructures was similarly improved with a pair of Au reflectors.[30] Despite the high light reflectivity, the construction of a metal reflector in photoreactors is prone to inducing large leakage noise current, leading to an unavoidable deterioration in the signal-to-noise ratio for information extraction in sensing networks.[31] A distributed Bragg reflector (DBR), a type of typical one-dimensional photonic crystal, consists of periodically repeated two dielectric layers with a large difference in the refractive index, which can be much more suitable for optoelectronic devices owing to its tunable reflect center wavelength and less electric noise interference.[32]

In this work, we propose novel 0D/2D ZnO quantum dot (QD)/MXene nanosheet (NS) composite thin film photodetectors fabricated on distributed Bragg reflector (DBR) substrates. The photogeneration of carriers within the composite thin films is radically intensified with the strong coupling between the DBR and MXene NSs, and a rapid transportation channel for photoactive carriers is constructed with uniformly distributed MXene NSs. Benefiting from the optic and electronic dual-effective enhancement effect, an excellent EQE of 489.1% and detectivity of 1.7×10^{13} jones are simultaneously obtained with the ZnO–MXene/DBR photodetector under 350 nm irradiation at a relatively low light power density of 0.16 mW cm^{-2}, offering a viable strategy to fabricate high-performance UV photodetectors with a long-term stability from a comprehensive perspective.

Results and discussion

The fabrication process of 0D/2D ZnO quantum dot (QD)/MXene nanosheet (NS) composite thin films on the distributed Bragg reflector (DBR) substrates is depicted in Fig. 1a. The as-synthesized spherical ZnO QDs were homogeneously dispersed in chloroform and methanol mixtures with an

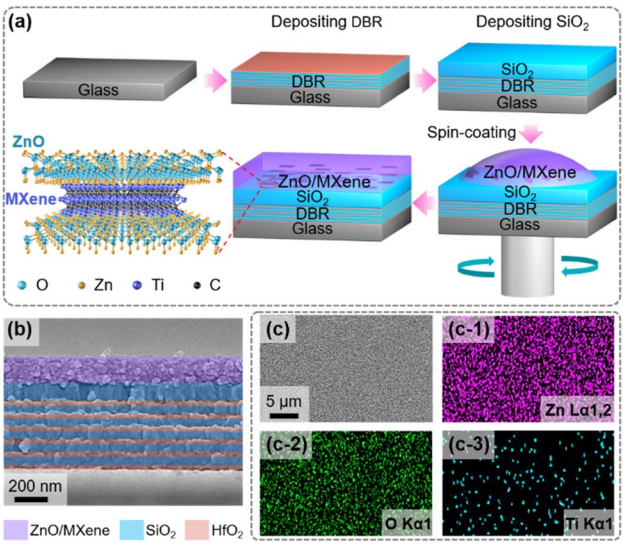

Fig. 1 (a) Schematic diagram for the manufacturing process of the 0D/2D ZnO quantum dot (QD)/MXene nanosheet (NS) composite thin films fabricated on the distributed Bragg reflector (DBR) substrate. (b) The scanning electron microscopy (SEM) cross-sectional image of the 0D/2D composite thin films on the DBR substrate. (c) The SEM top-view image and corresponding (c-1)–(c-3) energy-dispersive X-ray spectroscopy (EDS) images of the 0D/2D composite thin films.

average diameter of 5.4 nm as observed in Fig. S1a,† and the crystal lattice spacing distance of ~0.26 nm can be assigned to (002) planes for the wurtzite structure of ZnO as revealed in Fig. S1b.† The wurtzite crystal structure of ZnO QDs can be further confirmed by the six diffraction rings in the selected area electron diffraction (SAED) patterns as shown in Fig. S1c.† As shown in Fig. S1d,† the monolayer $Ti_3C_2T_x$ MXene NSs were obtained by the minimally intensive layer delamination method, and the shift of the (002) peak from ~9.6° to ~4.2° in the X-ray diffraction (XRD) patterns suggested the phase transition from MAX to MXene with an enlarged interplanar spacing according to Bragg's law as shown in Fig. S1e.† [33] As evidenced by the cross-sectional SEM image, the 0D/2D composite thin films with various concentrations of MXene NSs were deposited on the periodically arranged SiO_2/HfO_2 DBR substrate with a spacing layer of SiO_2. As shown by EDS spectra in Fig. S1f,† the Zn Lα, O Kα and Ti Kα peaks at 1.02, 0.53 and 0.45 keV were simultaneously detected for the 0D/2D composite thin films, and the uniform elementary distributions of Zn, O and Ti were verified by the EDS maps shown in Fig. 1c and (c-1)–(c-3).†

Fig. 2 shows the morphological development of ZnO QD thin films determined by the substrate and MXene NSs. For the samples fabricated on glass, the average grain size of the resulting ZnO QD thin films slightly increased from 23 to 25 nm with blending MXene NSs as shown in Fig. 2a and b, suggesting a neglectable effect on the morphology. Consequently, the surface root-mean-squared roughness (R_{RMS}) values acquired from atomic force microscope (AFM) images were comparable as revealed in Fig. 2d and e. As shown by the cross-sectional line-profiles in Fig. 2(d-1) and (e-1), the comparable surface morphologies of the thin films were equally evidenced by the

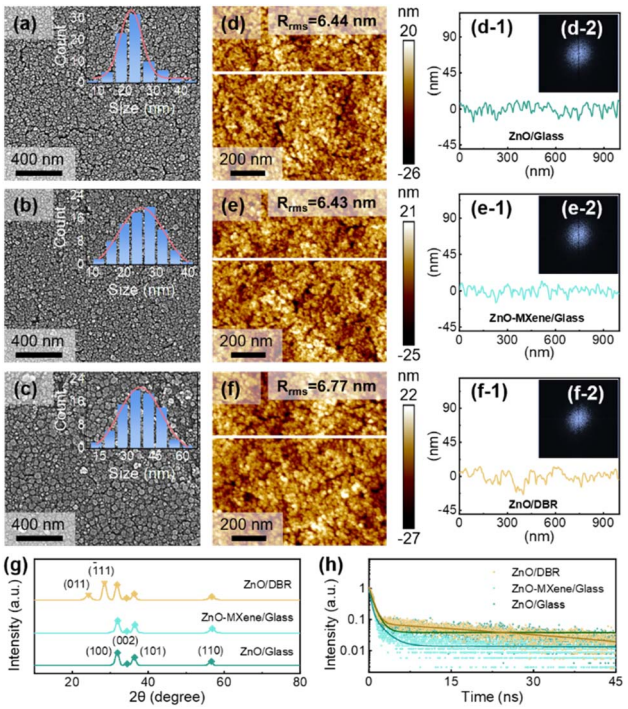

Fig. 2 (a)–(c) The SEM and (d)–(f) atomic force microscopy (AFM) images of pristine ZnO QD thin films on glass (ZnO/glass), ZnO QD/MXene NS thin films on glass (ZnO–MXene/glass), and pristine ZnO QD thin films on the DBR substrate (ZnO/DBR). (d-1)–(f-1) The corresponding cross-sectional line-profiles obtained from AFM images and (d-2)–(f-2) fast Fourier transform (FFT) power spectra of each sample. (g) X-ray diffraction (XRD) patterns and (h) time-resolved photoluminescence (TRPL) spectra of the samples.

height fluctuations, leading to identical height distribution throughout the whole surface as further confirmed by the symmetric spherical spots of a similar shape in fast Fourier transform (FFT) power spectra in Fig. 2(d-2) and (e-2). Meanwhile, a noticeable expansion of the average grain size from 23 to 37 nm was observed for the pristine ZnO QD thin films fabricated on glass and a DBR, and therefore the R_{RMS} increased from 6.44 to 6.77 nm as shown in Fig. 2c and f. As shown in Fig. 2(f-2), the spot size of the FFT power spectrum for the sample fabricated on the DBR slightly shrunk in comparison with the sample on glass due to the reduced height distribution frequency along with grain size expansion,[34] suggesting a sufficient growth of ZnO thin films on the DBR with a dense and uniform morphology as shown in Fig. S2a and b.† Likewise, 0D/2D ZnO QD/MXene NS composite thin films fabricated on a DBR (ZnO–MXene/DBR) exhibited an identical average grain diameter of 37 nm as observed in Fig. S2c.† As revealed by Fig. 2g, the (100), (002), (101), and (110) peaks of wurtzite ZnO were evenly witnessed with each sample,[35] and the peaks that occurred at 24.2° and 28.3° can be assigned to the (011) and ($\bar{1}$11) planes of HfO_2 in the DBR as shown in Fig. S2d.† [36] The time-resolved photoluminescence (TRPL) spectra of devices were recorded to investigate the photoinduced carrier dynamics as shown in Fig. 2h, and the fitting curves were obtained using bi-exponential decay functions:[37]

$$I(t) = A_1 \exp(-t/\tau_1) + A_2 \exp(-t/\tau_2) \quad (1)$$

where A_1 and A_2 denote the exponential weighting coefficient, and τ_1 and τ_2 are related to radiative and non-radiative recombination, respectively. The corresponding fitting coefficients of each sample are summarized in Table S1.† The short-lived component τ_1 of the samples ZnO QD thin films on glass (ZnO/glass), ZnO QD/MXene NS thin films on glass (ZnO–MXene/glass), and ZnO QD thin films on the DBR (ZnO/DBR) was 0.42, 0.34, and 0.71 ns, manifesting an intensified Auger recombination process in the presence of MXene NSs.[38] Meanwhile, the long-lived component τ_2 of the samples ZnO, ZnO–MXene/glass, and ZnO/DBR was 0.99 ns, 1.78 ns, and 45.73 ns, and a much longer τ_2 of the sample ZnO/DBR can be ascribed to the reduced boundaries along with grain agglomeration of ZnO thin films as confirmed by SEM images. As a result, the average lifetimes (τ_{ave}) of samples ZnO, ZnO–MXene/glass, and ZnO/DBR were 0.87 s, 1.09 s, and 38.94 s according to the equation:[39]

$$\tau_{ave} = A_1 \times {\tau_1}^2 + A_2 \times {\tau_2}^2/(A_1 \times \tau_1 + A_2 \times \tau_2) \quad (2)$$

The thickness effect of photoactive layers on the photoelectric performance of photodetectors was investigated to verify the optimized thickness of ZnO QD layers as shown in Fig. S3.† As shown in Fig. S3a,† the transmittance below bandgap (~350 nm) of ZnO QD thin films gradually declined from 50.1% to 4.7% with the increased thicknesses owing to the intensified absorption. With the increase of ZnO QD layers, the dark-current (I_{dark}) and photocurrent (I_{light}) gradually elevated at each bias due to the additional carriers as shown in Fig. S3b and c.† To evaluate the thickness effect on the photoelectric performance, the responsivity (R) and external quantum efficiency (EQE) were obtained using eqn (3) and are shown in Fig. S3d:† [40]

$$R = \frac{I_{light} - I_{dark}}{PS}, \ \mathrm{EQE} = R\frac{hc}{q\lambda} \quad (3)$$

where P, S, q, h, c and λ represent the optical power density, effective illuminated area, electron charge, Planck constant, speed of light, and wavelength of incident light, respectively. As shown in Table S2,† the R elevated from 10.1 to 75.7 mA W^{-1} depending on the ZnO layers, and the increase gradually became saturated due to the undesirable carrier trapping with extra defects for the thicker films,[41] which can be hardly diminished. Correspondingly, the EQE improved with an identical behavior from 3.6% to 26.8% as a function of ZnO QD layers. The specific detectivity (D^*) is regarded as an important figure-of-merit for photodetectors considering the noise effect, which can be expresses as:[42]

$$D^* = R\left(\frac{S}{2qI_{dark}}\right)^{1/2} \quad (4)$$

As summarized in Table S2,† the optimal D^* was obtained for the device fabricated with 2-layer ZnO QDs because of the increased noise current as evinced by the descending switching

ratio (SR) from 1.8×10^5 to 8.1×10^4, indicating a suitable thickness for the fabrication of photodetectors with a well-balanced performance.

The critical impediment for the device fabricated with 2-layer ZnO QD thin films was an insufficient light–matter reaction, which can be improved with multiple absorption by collecting back the transmitted light. Therefore, periodically arranged SiO_2/HfO_2 DBRs with various periods were designed, and simulated reflectance spectra are revealed in Fig. 3a. As presented in Fig. 3b, the experimentally highest reflectance of ~71.0% at 350 nm was obtained for the 5.5 period DBR. In order to fix the thickness of the isolating spacer (h_{SiO_2}), the electromagnetic (EM) field distribution in ZnO QD thin films fabricated on 5.5 period DBRs with a variation of h_{SiO_2} under 350 nm light illumination was investigated as shown in Fig. 3c, and the configurations of each device are revealed by SEM cross-sectional images in Fig. S4.† Obviously, the EM fields were boosted when the ZnO QD thin films were fabricated on DBRs than that on glass (D1), and the sample with a 100 nm isolating spacer (D3) exhibited a superior enhancement in EM fields within the ZnO QD thin films. Correspondingly, the absorption of ZnO QD thin films at 350 nm was obviously enhanced for the sample D3 as evidenced by the theoretically simulated absorption spectra in Fig. S5a.† As revealed in Fig. S5b–d,† the experimental absorption spectra of samples were calculated according to the transmittance and reflectance spectra, and the optimized absorption of ZnO QD thin films at 350 nm was similarly witnessed with the sample D3. As shown in Fig. 3d, the I_{dark} of devices fabricated on the DBRs was somewhat elevated compared to that of the device fabricated on glass at each bias arising from the improved crystallinity as mentioned above,[43] and the evolution of I_{light} was consistent with the light absorption as discussed. As a result, the device D3 exhibited an apparently enhanced R and EQE of 490.4 mA W^{-1} and 173.9% as shown in Fig. 3e and Table 1. An optimized D^* of 6.4×10^{12} jones was likewise obtained for the device with a h_{SiO_2} of 100 nm, and the relatively higher D^* of the device D1 can be attributed to the lower I_{dark} than the devices fabricated on DBRs.

To develop a comprehensive perspective on the 0D/2D composite thin film photodetectors, a systematic comparison of the photoelectronic performance of the photodetectors with diverse configurations: ZnO/glass (D1), ZnO/DBR (D3), ZnO–MXene/glass (D6), and ZnO–MXene/DBR (D7) was performed. The corresponding configuration of the device D7 is depicted in Fig. 4a. As shown in Fig. 4b, the device fabricated on DBRs exhibited elevated I_{dark} at each bias voltage owing to the improved crystallinity, and comparatively higher I_{dark} was always observed for the device blended with MXene NSs regardless of substrates due to the improved conductivity.[44] Meanwhile, the charge-transfer resistance (R_{ct}) of the pristine ZnO and ZnO–MXene thin films was 8.49 and 8.11 GΩ according to the Nyquist plots in Fig. 4c, confirming the accelerated charge transportation in the presence of MXene NSs. As revealed in Fig. 4d, the I_{light} for the sample with MXene NSs was noticeably elevated under 350 nm light illumination, which can be ascribed to the boosted light absorption *via* concentrating incident light with the spontaneously collective free-electron oscillation of MXene NSs as revealed in Fig. S6a.† [45] As shown in Fig. S6b,† the near-band edge excitonic emission (NBE) band at 378 nm[46] and the defect related emission band at 470 nm[47] were equally witnessed for the ZnO QD and ZnO QD/MXene NS composite thin films. Similarly, the intensified localized EM fields in the presence of MXene NSs can be also proved by the increased NBE band inducing by the enhanced radiative recombination, resulting in a much more noticeable increase of I_{light} from 434.3 nA to 12.0 μA at 10 V owing to the strong coupling between MXene NSs and DBRs. Thus, superior performance including R (0.93 A W^{-1}), EQE (327.9%), and D^* (1.16×10^{13} jones) was simultaneously achieved with the device ZnO–MXene/DBR as shown in Fig. 4e and f. The response time including the rise time (t_{rise}) and decay time (t_{decay}) for the photodetectors is shown in Fig. S7.† The slightly elongated response duration for the devices fabricated on the DBR was possibly induced by the reduced surface defect density with improved grain growth as proved in previous work,[48] and the rapid carrier transportation with MXene NSs can offer an

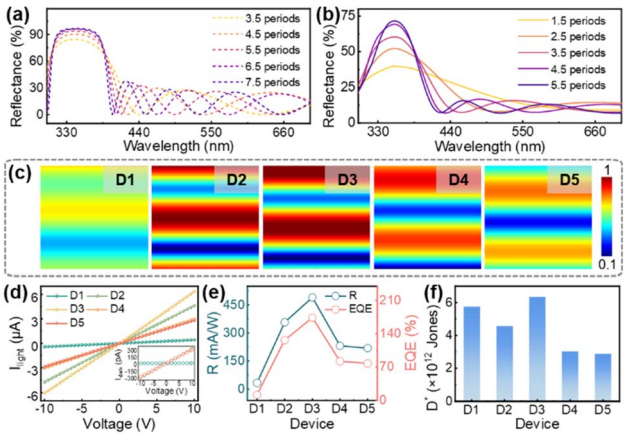

Fig. 3 (a) The simulated and (b) experimental reflectance (R) spectra of DBRs with different periods. (c) Electromagnetic field distribution in ZnO layers for the devices fabricated on glass (D1) and on DBRs with various thicknesses of SiO_2 isolating spacers (h_{SiO_2}): (D2: 80 nm, D3: 100 nm, D4: 120 nm, and D5: 140 nm). (d) Photocurrent (I_{light}) and (inset) dark-current (I_{dark}) of the devices. (e) Responsivity (R), external quantum efficiency (EQE), and (f) normalized detectivity (D^*) of each device.

Table 1 R, EQE, D^*, and switching ratio (SR) of the devices

Device	R (mA W^{-1})	EQE	D^* ($\times 10^{12}$ jones)	SR ($\times 10^4$)
D1	33.5	11.9%	5.7	25
D2	356.9	126.5%	4.6	1.5
D3	490.4	173.9%	6.4	2.1
D4	231.0	81.9%	3.0	1.0
D5	218.6	77.5%	2.9	0.98
D6	285.1	101.1%	9.1	7.6
D7	925.0	327.9%	11.6	3.8

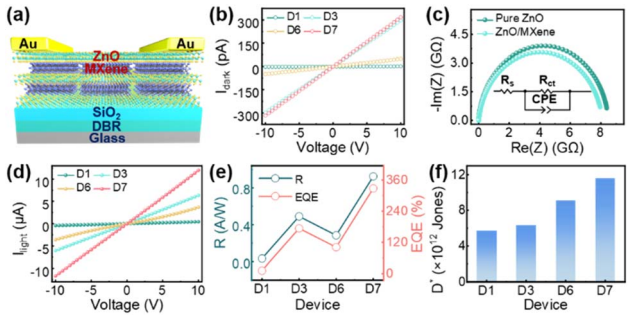

Fig. 4 (a) Scheme for the configuration of the ZnO QD/MXene NS thin films on DBRs (ZnO–MXene/DBR). (b) I_{dark} of the photodetectors: ZnO/glass (D1), ZnO/DBR (D3), ZnO–MXene/glass (D6), and ZnO–MXene/DBR (D7). (c) Nyquist plots of ZnO and ZnO/MXene. (d) I_{light} of the photodetectors. (e) R, EQE, and (f) D^* of the devices.

effective way to improve the response time irrespective of substrates. The enhancement mechanism was theoretically investigated based on the optical and electrical simulation of the 0D/2D composite thin films as shown in Fig. 5 and S8.† As shown in Fig. 5a and b, the incident photons can be concentrated around the surface of MXene NSs induced by a spontaneously photoexcited EM field,[49] and the photoexcited EM field was significantly boosted with the DBR, which can effectively compensate for the limited vertical-dimension of MXene NSs for light confinement. Apart from the absorption enhancement, the presence of MXene NSs can be also beneficial for carrier transportation within the 0D/2D composite thin films. As depicted in Fig. 5c, the MXene possessed a relatively lower work function (W_M = ~4.3 eV) than ZnO (W_Z = ~5.2 eV), and thus a built-in electric field was spontaneously formed at the heterointerface between MXene and ZnO as shown in Fig. 5d. As revealed in Fig. 5e and f, the potential distribution within the ZnO thin films was correspondingly changed by blending with MXene NSs, and the electron transportation pathway can in turn be constructed in the 0D/2D composite thin films as observed in Fig. S8,† which was consistent with the behavior of the photodetectors.

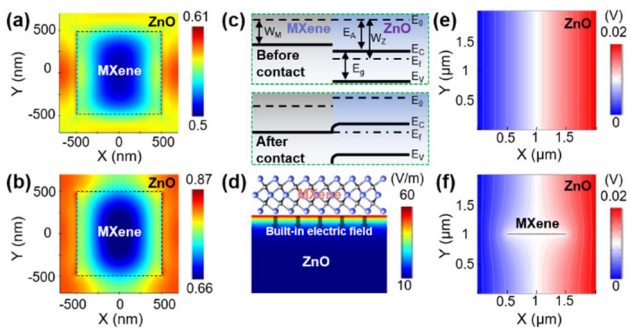

Fig. 5 Electromagnetic field distribution of ZnO QD/MXene NS nanocomposites on (a) glass and (b) a DBR. (c) Energy-band diagram of ZnO and MXene before and after coming into contact. (d) Built-in electric field distribution in ZnO at the interface of ZnO and MXene. Simulation of the potential distribution of (e) pristine ZnO and (f) ZnO QD/MXene NS nanocomposites.

To thoroughly evaluate the enhancement effect, the photoelectric performance of the devices was systematically investigated at different wavelengths and light power densities as shown in Fig. 6. As presented in Fig. 6a, the optimal I_{light} of the device D7 was always obtained under 350 nm light illumination at each bias voltage, and comparable behavior was witnessed for the photodetectors regardless of the configuration as shown in Fig. S9.† As a result, the R of the device D7 was superior to that of each detector throughout the spectral ranges between 300 and 400 nm as shown in Fig. 6b. Under 350 nm light illumination, the transient response of the device D7 was obviously higher than that of the device D1 at various light power densities as revealed in Fig. 6c. The relationship between I_{light} and incident light power density can be described as:[50]

$$I_{light} = AP^{\alpha} \quad (5)$$

where A is a fitting constant, P is the incident light power density, and α is the Duane plot slope. As shown in Fig. S10a and b,† the α for the devices D1 and D7 was larger than 0.5, suggesting relatively lower defect densities in pristine ZnO and 0D/2D composite thin films.[51] Meanwhile, the α of the device D7 (α = 0.73) was slightly lower than that of the device D1 (α = 0.91), which can be induced by the saturated generation of photo-excited carriers under the further enhanced light power owing to the intensified light utilization.[52] The light power dependent behavior was evenly witnessed with all the figure-of-merits (R, EQE, and D^*) for the devices D1 and D7 due to the photoinduced absorption–desorption process within ZnO as a function of light intensities,[53] and optimized R (1.4 A W^{-1}), EQE (489.1%), and D^* (1.7×10^{13} jones) were eventually obtained with the device D7 at a light power density of 0.16 mW cm^{-2} as shown in Fig. 6d–e, S10c and d.† The EQE of the device D7 was above 1, which can be induced by the photoconductive gain.[54] Particularly, R, EQE and D^* are reversely proportional to the light power, which can be widely witnessed with various photodetectors.[55,56] The comparison of the performance of state-of-the-art UV ZnO photodetectors with various configurations is summarized in Table 2,[57–66] and the ZnO–MXene/DBR photodetector (D7) proposed in this work exhibited an

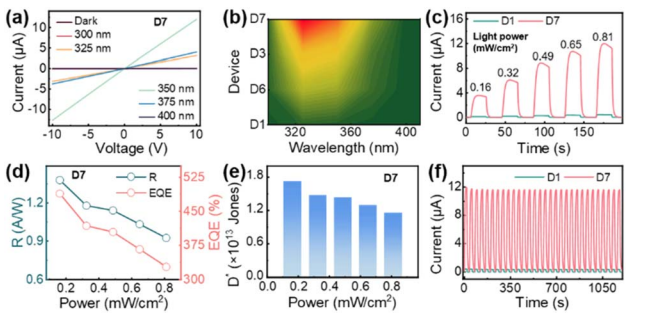

Fig. 6 (a) The spectral I–V curves of the device D7. (b) Contour maps of spectral responsivity for each device at an identical voltage of 10 V. (c) Transient response of the devices under various light power densities at 10 V. (d) R, EQE, and (e) D^* of the device D7 under different light power densities. (f) Multiple-period response of the devices.

Table 2 Photoresponse comparison of ZnO UV photodetectors with various configurations reported in recent years

Device	Measurement conditions	R [mA W^{-1}]	D^* [jones]	t_{rise} [s]	t_{decay} [s]	Number of cycles	Ref.
ZnO QDs/CuO micro-pyramid PD	244 nm, 2.1 mW cm^{-2},1 V	956	7.72 × 10^{11}	—	—	—	57
$BaTiO_3$–ZnO PD	370 nm, 3 V	1.28	2.7 × 10^{11}	—	—	—	58
ZnO fibril-like clustered microwire PD	405 nm, 17 mW cm^{-2}, 8 V	716	6.72 × 10^{10}	4	5	—	59
ZnO homojunction nanofiber PD	360 nm, 0.5 mW cm^{-2}, 0 V	1.28	—	3.9	4.7	16	60
$Cs_3Cu_2I_5$/ZnO flexible PD	280 nm, 4V	314	1.26 × 10^{11}	—	—	—	61
Ag/$CsPbBr_3$ QD/ZnO NRs/Ag PD	365 nm, 0.15 mW cm^{-2}, 10 V	320	—	—	—	—	62
Self-powered ZnO UV photodetector array	365 nm, 2.3 mW cm^{-2}	47.4	3.55 × 10^{9}	—	—	25	63
Cu NS/ZnO QD hybrid architecture PD	365 nm, 620 μW cm^{-2}, 10 V	—	—	7.4	29	50	64
ZnO/GNDA PD	360 nm, 0.403 mW cm^{-2}, 5 V	22.55	—	—	11	—	65
Cu/h-BN/ZnO/Cu NW PD	265 nm, 2 μW cm^{-2}, −7 V	700 × 10^{3}	5.4 × 10^{12}	—	—	250	6
ZnO–MXene/DBR PD	350 nm, 0.16 mW cm^{-2}, 10 V	1400	1.7 × 10^{13}	3.79	1.93	30	This work

excellent photoelectric performance with a relatively fast response time among all the devices. As presented in Fig. 6f, the outstanding stability of the devices D1 and D7 was further confirmed within 30 testing cycles, manifesting a versatile strategy with a dual-effective enhancement effect from optic and electronic perspectives for the large-scale manufacture of high-performance UV photodetectors. An optical communication system based on the device D7 is shown in Fig. 7. As presented in Fig. 7a, the encoded signal drove the UV light, and then the transmitted signals can be directly detected by the device D7 and recorded by a Keithley 4200. The recorded signal is shown in Fig. 7b. To further explore the potential application of devices, a complete optical communication system was established as shown in Fig. 7c. Initially, the character string "WUT" was encoded as a binary code ("0101 0111" represents "W", "0101 0101" represents "U", and "0101 0100" represents "T"). The function generator recorded the binary code and drove the UV light. Then the modulated optical signal was detected by the device D7. The output signal was amplified and demodulated. And the character string "WUT" was displayed on the electronic display screen. The test of the corresponding optical communication system is shown in Video 1.† The results of the optical communication system exhibited a promising prospect in the construction of optical communication networks.

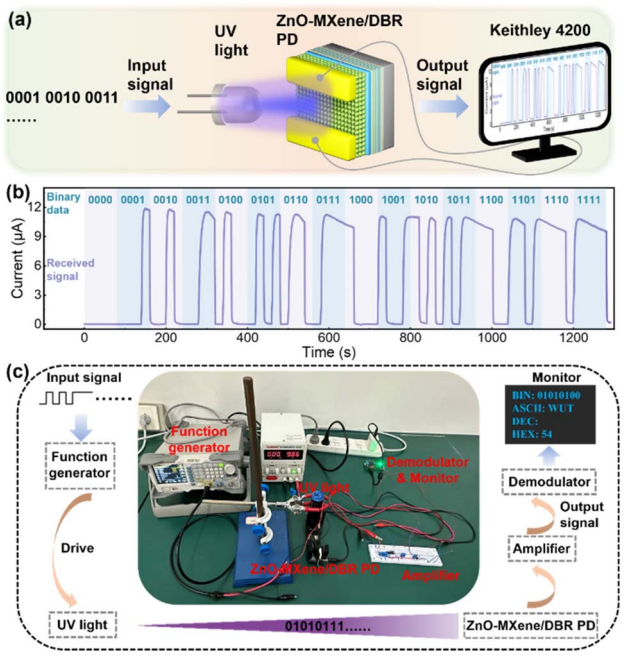

Fig. 7 (a) Schematic diagram and (b) received signal of the optical modulation test of the device D7. (c) Optical communication system based on the device D7.

Conclusions

In summary, we have successfully fabricated 0D/2D ZnO QD/MXene NS composite thin films on DBR substrates with an optimized performance from optic and electronic perspectives. The morphological and optical effects on the 0D/2D ZnO QD/MXene NS composite thin films were systematically investigated depending on the repeated period of the DBR, and the strong coupling of MXene NSs and the DBR provided an efficacious for the inherent discrepancy between light absorption and carrier transportation within the composite thin films. The photoinduced carrier extraction was improved with a hetero-interface built-in electric field from MXene to ZnO, and the carrier transfer was subsequently accelerated as theoretically evidenced by electrical simulation. As a consequence, a series of exceptional figure-of-merits were simultaneously obtained with the ZnO–MXene/DBR photodetector under 350 nm light illumination at a relatively low light power density of 0.16 mW cm^{-2}, resulting in optimized EQE and D^* with the values of ~489.1% and ~1.7 × 10^{13} jones at 10 V. This work not only enriched the strategy for insufficient light utilization in low-dimensional photoactive layers without introducing extra noise, but also shed light on the development of high-performance UV photodetectors in the future.

Experimental section

Device fabrication

Fabrication of devices with different ZnO QD layers. The synthesis methods of ZnO QDs and MXene NSs were presented in our previous work.[67] ZnO with different layers (1 layer, 2

layers, 3 layers, and 4 layers) was deposited through spin-coating at 2500 rpm for 60 s on glass substrates. Each thin film is annealed in a furnace (KSL-1200X, China) at 250 °C for 60 minutes at a heating rate of 8.3 °C min^{-1}. Au electrode pairs with a spacing of 200 μm were deposited on ZnO through a magnetron sputtering system (Sputtering 500C, China) at a rate of 0.80 Å s^{-1} under 2 Pa with a direct current source of 30 mA.

Fabrication of ZnO/DBR. The DBR consisted of periodically arranged SiO_2 and HfO_2 thin films. Each dielectric film was deposited through a radio frequency (RF) magnetron sputtering system (Sputtering 500C, China) under 0.5 Pa with an Ar/O_2 flow ratio of 4. The RF power and deposition rate were 150 W and 0.20 Å s^{-1} for SiO_2 and 100 W and 0.57 Å s^{-1} for HfO_2. SiO_2 isolating spacers with various thicknesses were deposited on the DBR to adjust the position of light interference in ZnO. 2 layers of ZnO thin films were deposited on SiO_2 isolating spacers by spin-coating at 2500 rpm for 60 s, and then annealed at 250 °C for 60 minutes. Finally, Au electrode pairs were deposited on ZnO.

Fabrication of ZnO–MXene/DBR. The DBR and SiO_2 isolating spacers were deposited on glass through the RF magnetron sputtering method. ZnO QD/MXene NS composite solution with an MXene NS concentration of 0.1 mg mL^{-1} was spin-coated on SiO_2 at 2500 rpm for 60 s according to previous work.[66] The sample was then annealed at 250 °C for 60 minutes and a pair of Au electrodes were deposited on ZnO.

Device characterization

The morphologies of devices were characterized by scanning electron microscopy (SEM, Hitachi SU8010, Japan) and atomic force microscopy (AFM, Bruker Dimension Icon, Germany). Elemental analysis of the ZnO/MXene thin film was carried out with energy-dispersive X-ray spectroscopy (EDS) coupled with SEM. The crystal structures of the devices were confirmed using X-ray diffraction (XRD, Rigaku SmartLab SE, Japan) with Cu Kα radiation at a scan rate of 5° min^{-1}. The effects of the substrate and MXene on the lifetime of ZnO thin films were determined by time-resolved photoluminescence (TRPL, FLS1000, England) with an excitation wavelength of 340 nm, monitoring the emission at 378 nm. Images of ZnO QDs and the corresponding SAED patterns were taken by transmission electron microscopy (TEM, FEI Tecnai G2 F20, America). The reflectance spectra, transmittance spectra and absorbance spectra of devices were recorded with a UV-vis-NIR spectrophotometer (UV-2600, Japan). The PL spectra of devices excited by a light source of 325 nm were tested by using a spectrofluorophotometer (RF-6000, Japan). A semiconductor parameter analyzer (Keithley 4200, America) equipped with a xenon lamp (CME-OPS1000, China) was applied to characterize the photoelectric performance of the devices.

Optical and electrical simulation

Commercial FDTD solution (Lumerical) software was adapted to confirm the reflectance, absorption spectra and the electric field distribution. For the reflectance spectra of the DBR structure, the height of SiO_2 and HfO_2 was set at 59.1 nm and 42.9 nm respectively according to the formula: $h = \lambda/4n$. The refractive index n and extinction coefficient k of SiO_2 and HfO_2 were obtained from references.[67,68] The effects of various SiO_2 thicknesses on the electric field distribution and the corresponding absorption spectra in ZnO thin films were confirmed by adding SiO_2 isolating spacers between ZnO and the DBR. The height of 2-layer ZnO thin films (~160 nm) was probed by using a stylus profiler (KLA-Tencor D120, America). And we simulated the ZnO thin film without the DBR as a pristine group. In addition, we designed a FDTD simulation of the ZnO/MXene composite thin film with and without the DBR structure to verify the intensified near-surface electric field of a single MXene nanosheet. The width and length were set at 1 μm with a thickness of 1 nm. A plane-wave source with a wavelength of 350 nm and polarized E-field direction parallel to the x-axis was applied to structures. The boundary conditions were periodical for the x-axis and y-axis, and a perfectly matched layer (PML) for the z-axis. The current density and potential distribution of ZnO/MXene composite thin films were simulated in COMSOL Multiphysics with a 2-dimensional space and EC electric field. The conductivity (σ) and relative permittivity (ε_r) of ZnO were set to be 1.32×10^{-3} S m^{-1} and 4, respectively.[69,70] For the MXene, σ and ε_r were set to be 2.4×10^5 S m^{-1} and 3.5, respectively.[71] The length and thickness of MXene were set to be 1 μm and 1 nm, respectively. The voltages of 0 V and 0.02 V were set to boundaries of ZnO. The built-in electric fields near the interface of ZnO and MXene were simulated in COMSOL Multiphysics with a 2-dimensional space and semiconductor module. The bandgap, electron affinity and work function of ZnO were set to be 3.37 eV, 4.3 eV and 5.2 eV respectively.[72–74] As for MXene, the work function was set to be 4.3 eV.[75]

Author contributions

Ming-Yu Li proposed the original idea and supervised the project. Zhenpeng Cheng and Zeping Li fabricated the samples and wrote the manuscript. Xumin Ding and Hao Xu partially participated in the design and fabrication of the DBR structure. Haifei Lu and Xiaoyan Wen performed the optical characterization for each sample. Sisi Liu and Jihoon Lee revised the manuscript. All authors discussed the results and commented on the manuscript.

Conflicts of interest

There are no conflicts to declare.

Acknowledgements

This research was supported by the National Key Research and Development Program of China (2021YFF0603500), National Natural Science Foundation of China (Grant No. 62204180, 11974266, and 62075174), National Research Foundation of Korea (Grant No. NRF-2022R1H1A2091290, NRF-2019R1A2C4069438, and NRF-2018R1A6A1A03025242), Science Foundation of Donghai Laboratory (DH-

2022KF01007), and Fundamental Research Funds for the Central Universities (WUT:2021VA056).

Notes and references

1 M. Kumar, J.-Y. Park and H. Seo, *ACS Appl. Mater. Interfaces*, 2021, **13**, 12241–12249.
2 T. M. H. Nguyen and C. W. Bark, *ACS Appl. Mater. Interfaces*, 2022, **14**, 45573–45581.
3 L. Ghorbani and S. Nasirian, *Appl. Surf. Sci.*, 2020, **527**, 146786.
4 L. Yang, W.-L. Tsai, C.-S. Li, B.-W. Hsu, C.-Y. Chen, C.-I. Wu and H.-W. Lin, *ACS Appl. Mater. Interfaces*, 2019, **11**, 47054–47062.
5 Q. Li, J. Meng, J. Huang and Z. Li, *Adv. Funct. Mater.*, 2021, **32**, 2108903.
6 G. Liu, H. Chen, S. Lu, L. Liu, X. Xu, L. Shi, B. Chen, B. Guo, P. Shen, Y. Cai, H. Zhang, Y. Tang, A. M. Soomro, F. Xu, X. Chen, T. Zheng, J. Li, S. Li, D. Cai and J. Kang, *Small*, 2022, **18**, 2200563.
7 H. Ferhati, F. Djeffa, A. Bendjerad, L. Foughali, A. Benhaya and A. R. Saidi, *J. Alloys Compd.*, 2022, **907**, 164464.
8 D. Wu, Z. Zhao, W. Lu, L. Rogée, L. Zeng, P. Lin, Z. Shi, Y. Tian, X. Li and Y. H. Tsang, *Nano Res.*, 2021, **14**, 1973–1979.
9 J. Li, X. Xi, S. C. Lin, Z. Ma, X. Li and L. Zhao, *ACS Appl. Mater. Interfaces*, 2020, **12**, 11965–11971.
10 Z.-L. Li, Z. Li, C. Zuo and X. Fang, *Adv. Mater.*, 2022, **34**, 2109083.
11 Z. Li, T. Yan and X. Fang, *Nat. Rev. Mater.*, 2023, **8**, 587–603.
12 W. Song, J. Chen, Z. Li and X. Fang, *Adv. Mater.*, 2021, **33**, 2101059.
13 A. Kumar, X. Li, Y. Du, Y. Geng and X. Hong, *Appl. Surf. Sci.*, 2020, **509**, 144770.
14 K. Singh, N. Berwal, I. Rawal, S. Dahiya, R. Punia and R. Dhar, *J. Alloys Compd.*, 2018, **768**, 978–990.
15 Y. Wang, L. Zhu, Y. Feng, Z. Wang and Z. L. Wang, *Adv. Funct. Mater.*, 2018, **29**, 1807111.
16 M. A. Khan, M. K. Singha, K. K. Nanda and S. B. Krupanidhi, *Appl. Surf. Sci.*, 2020, **505**, 144365.
17 K.-H. Kim, X.-Y. Li, G. Li, T. Ji, F. Ai, J. Wu, E. Ha and J. Hu, *Adv. Funct. Mater.*, 2021, **31**, 2011284.
18 Y.-L. Shi, Q. Lv, Y. Tao, Y. Ma and X. Wang, *Angew. Chem., Int. Ed.*, 2022, **61**, 202008768.
19 H. Yuan, A. Alateeqi, J. Yuan, Y.-X. Wang, H. Liu, J. Fang, C. Tang, X. Yan, H. Cai, Y. Gu, S. J. Pennycook, J. Tao and D. Zhao, *Adv. Mater.*, 2019, **31**, 1807161.
20 Y. Gao, J. Zheng, W. Chen, L. Yuan, Z. L. Teh, J. Yang, X. Cui, G. Conibeer, R. Patterson and S. Huang, *J. Phys. Chem. Lett.*, 2019, **10**, 5729–5734.
21 W. Ouyang, F. Teng, J. He and X. Fang, *Adv. Funct. Mater.*, 2019, **29**, 1807672.
22 H. Chen, K. Liu, L. Hu, A. A. Al-Ghamdi and X. Fang, *Mater. Today*, 2015, **18**, 493–502.
23 X. Jiang, D. Yin, M. Yang, J. Du, W. Wang, L. Zhang, L. Yang, X. Han and B. Zhao, *Appl. Surf. Sci.*, 2019, **487**, 938–944.
24 Y. Chen, Y. Ge, W. Huang, Z. Li, L. Wu, H. Zhang and X. Li, *ACS Appl. Nano Mater.*, 2020, **3**, 303–311.
25 H. Li, Z. Li, S. Liu, M. Li, X. Wen, J. Lee, S. Lin, M.-Y. Li and H. Lu, *J. Alloys Compd.*, 2022, **895**, 162570.
26 J. Zhang, N. Kong, S. Uzun, A. Levitt, S. Seyedin, P. A. Lynch, S. Qin, M. Han, W. Yang, J. Liu, X. Wang, Y. Gogotsi and J. M. Razal, *Adv. Mater.*, 2020, **32**, 2001093.
27 W. Ouyang, J. Chen, J.-H. He and X. Fang, *Adv. Electron. Mater.*, 2020, **6**, 2000168.
28 T.-Y. Zhang, H. Wang, J. Tong, J. Zhang, X. Wang and Y. Zeng, *Compos. Commun.*, 2022, **33**, 101235.
29 M. R. Lien, N. Wang, J.-B. Wu, A. Soibel, S. D. Gunapala, H. Wang and M. L. Povinelli, *Nano Lett.*, 2022, **22**, 8704–8710.
30 F. Wang, Z. Liu, T. Zhang, M. Long, X. Wang, R. Xie, H. Ge, H. Wang, J. Hou, Y. Gu, X. Hu, Z. Song, S. Wang, Q. Dong, K. Liao, Y. Tu, T. Han, F. Li, Z. Zhang and X. Hou, *Adv. Mater.*, 2022, **34**, 2203283.
31 T. Hemati and B. Weng, *J. Appl. Phys.*, 2018, **124**, 2203283.
32 F. Zhao, A. Ren, P. Li, Y. Li, J. Wu and Z. M. Wang, *ACS Nano*, 2022, **16**, 7116–7143.
33 J. He, P. Wu, L. Chen, H. Li, M. Hua, L. Lu, Y. Wei, Y. Chao, S. Zhou and W. Zhu, *Chem. Eng. J.*, 2021, **416**, 129022.
34 M. Hoang Tran, T. Park and J. Hur, *Appl. Surf. Sci.*, 2021, **539**, 148222.
35 K. Benyahia, F. Djeffal, H. Ferhati, A. Bendjerad, A. Benhaya and A. Saidi, *J. Alloys Compd.*, 2021, **859**, 158242.
36 S. Li, Y. Zhang, D. Yang, W. Yang, X. Chen, H. Zhao, J. Hou and P. Yang, *Phys. B*, 2020, **584**, 412065.
37 S. Liu, K. Xiong, K. Wang, G. Liang, M. Li, H. Tang, X. Yang, Z. Huang, L. Lian, M. Tan, K. Wang, L. Gao, H. Song, D. Zhang, J. Gao, X. Lan, J. Tang and J. Zhang, *ACS Nano*, 2021, **15**, 3376–3386.
38 V. S. Chirvony, S. Gonzalez-Carrero, I. Suárez, R. E. Galian, M. Sessolo, H. J. Bolink, J. P. Martínez-Pastor and J. Pérez-Prieto, *J. Phys. Chem. C*, 2017, **121**, 13381–13390.
39 S. Park, B. J. Kim, T. Y. Kim, E. Y. Jung, K.-M. Lee, J.-A. Hong, W. Jeon, Y. Park and S. J. Kang, *J. Mater. Chem. C*, 2021, **9**, 2550–2560.
40 S. Liu, H. Li, H. Lu, Y. Wang, X. Wen, S. Deng, M. Li, S. Liu, C. Wang and X. Li, *Nanomaterials*, 2022, **12**, 4217.
41 M. Saleem, W. A. Farooq, M. I. Khan, M. N. Akhtar, S. U. Rehman, N. Ahmad, M. Khalid, M. Atif, M. A. AlMutairi and M. Irfan, *Micromachines*, 2019, **10**, 819.
42 W. Wu, X. Han, J. Li, X. Wang, Y. Zhang, Z.-Y. Huo, Q. Chen, X. Sun, Z. Xu, Y. Tan, C. Pan and A. Pan, *Adv. Mater.*, 2021, **33**, 2006006.
43 J. H. Mun, H.-J. Lee, S. H. Lee, T. Yoon, S. H. Han and D. H. Kim, *ACS Appl. Nano Mater.*, 2020, **3**, 10922–10930.
44 E. Pargoletti, U. H. Hossain, I. Di Bernardo, H. Chen, T. Tran-Phu, J. Lipton-Duffin, G. Cappelletti and A. Tricoli, *Nanoscale*, 2019, **11**, 22932–22945.
45 S. Liu, M.-Y. Li, D. Su, M. Yu, H. Kan, H. Liu, X. Wang and S. Jiang, *ACS Appl. Mater. Interfaces*, 2018, **10**, 32516–32525.
46 L. Li, C. Yao, W. Li, K. Jiang, Z. Hu, N. Xu, J. Sun and J. Wu, *J. Phys. Chem. C*, 2021, **125**, 13732–13740.
47 S. Pal, P. Barik and M. Pradhan, *Mater. Today Commun.*, 2021, **28**, 102713.

48 Z. Li, X. Yu, Y. Zhu, S. Liu, X. Wen, H. Lu, C. Wang, X. Li, M.-Y. Li and Y. Yang, *Appl. Surf. Sci.*, 2022, **582**, 152352.
49 S. Liu, M.-Y. Li, J. Zhang, D. Su, Z. Huang, S. Kunwar and J. Lee, *Nano-Micro Lett.*, 2020, **12**, 114.
50 J. Wu, F. Wang, H. Li, S. Yang, P. Li, Y. Zhao, Y. Li and T. Zhai, *Small*, 2021, **18**, 2104244.
51 W. Kong, C. Zhao, T. Huang, L. Xiuyun, J. Xing, Z. G. Yu, P. Yang, W. Li and W. Yu, *ACS Appl. Mater. Interfaces*, 2022, **14**, 28154–28162.
52 M. Li, S. Liu, Z. Huang, Y. Ai, K. Shen, H. Lu and J. Wu, *ACS Appl. Mater. Interfaces*, 2021, **13**, 35972–35980.
53 V. Q. Dang, T. Q. Trung, D.-I. Kim, L. T. Duy, B.-U. Hwang, D.-W. Lee, B.-Y. Kim, L. D. Toan and N.-E. Lee, *Small*, 2015, **11**, 3054–3065.
54 B. Cook, M. Gong, D. Ewing, M. Casper, A. Stramel, A. Elliot and J. Wu, *ACS Appl. Nano Mater.*, 2019, **2**, 3246–3252.
55 G. Kumar, N. Prakash, M. Singh, A. Chakravorty, D. Kabiraj, S. P. Singh, P. Pal and S. P. Khanna, *ACS Appl. Electron. Mater.*, 2019, **1**, 1489–1497.
56 Z. Wang, M. Li, X. Gao and Z. Zhang, *ACS Appl. Electron. Mater.*, 2019, **1**, 2236–2243.
57 N. Alwadai, S. Mitra, M. N. Hedhili, H. Alamoudi, B. Xin, N. Alaal and I. S. Roqan, *ACS Appl. Mater. Interfaces*, 2021, **13**, 33335–33344.
58 Y. Zhang, X. Zhao, J. Chen, S. Liu, W. Yang and X. Fang, *Adv. Funct. Mater.*, 2019, **30**, 1907650.
59 Y. Purusothaman, N. R. Alluri, A. Chandrasekhar, V. Vivekananthan and S.-J. Kim, *Small*, 2018, **14**, 1703044.
60 Y. Ning, Z.-M. Zhang, F. Teng and X. Fang, *Small*, 2018, **14**, 1703754.
61 X. Zhao, Y. Tao, J. Dong, Y. Fang, X. Song and Z. Yan, *ACS Appl. Mater. Interfaces*, 2022, **14**, 43490–43497.
62 J.-F. Tang, Y.-D. Sie, Z. Tseng, J. Lin, L.-C. Chen and C.-L. Hsu, *ACS Appl. Nano Mater.*, 2022, **5**, 7237–7245.
63 Y. Ji, L. Wu, Y. Liu and Y. Yang, *Nano Energy*, 2021, **89**, 106449.
64 M. Li, M. Yu, D. Su, J. Zhang, S. Jiang, J. Wu, Q.-P. Wang and S. Liu, *Small*, 2019, **15**, 1901606.
65 R. Tang, S. Han, F. Teng, K. Hu, Z. Zhang, M. Hu and X. Fang, *Adv. Sci.*, 2017, **5**, 1700334.
66 M. Li, Z. Li, H. Li, S. Liu, H. Lu, X. Wen and Y. Yang, *ACS Appl. Nano Mater.*, 2021, **4**, 13674–13682.
67 L. V. Rodríguez-de Marcos, J. I. Larruquert, J. A. Méndez and J. A. Aznárez, *Opt. Mater. Express*, 2016, **6**, 3622.
68 A. Zahoor, C. Xu, T. Shahid, M. A. Anwar and Z. Song, *Vacuum*, 2022, **197**, 110824.
69 F. Yang, Y. Xu, M. Gu, S. Zhou, Y. Wang, K. Lu, Z. Liu, X. Ling, Z. Zhu, J. Chen, Z. Wu, Y. Zhang, Y. Xue, F. Li, J. Yuan and W. Ma, *J. Mater. Chem. A*, 2018, **6**, 17688–17697.
70 J.-W. Yang, J. Lee, J. Lee and W. Yi, *ACS Appl. Mater. Interfaces*, 2018, **10**, 25311–25320.
71 E. Li, C. Gao, R. Yu, X. Wang, L. He, Y. Hu, H. Chen, H. Chen and T. Guo, *Nat. Commun.*, 2022, **13**, 2898.
72 D. Kuang, Y. Li, Y. Gao, J. Guo, X. Li, S. Xu, B. Liu, X. Liu, Y. Zhang and Z. Yu, *J. Alloys Compd.*, 2022, **899**, 163185.
73 H. J. Choi, S. Seo, J. H. Lee, S. K. Hong, J. Song, S.-K. Kim, S. Yim, K. Lee, S.-J. Park and S. Lee, *J. Mater. Chem. C*, 2018, **6**, 6014–6022.
74 N. Abutaha, A. Hezam, F. A. Almekhlafi, A. M. N. Saeed, K. Namratha and K. Byrappa, *Appl. Surf. Sci.*, 2020, **527**, 146893.
75 R. Hou, S. Zhang, P. Zhang, Y. Zhang, X. Zhang, N. Li, Z. Shi and G. Shao, *J. Mater. Chem. A*, 2020, **8**, 25255–25267.